

Title: Metallo-Fluorocarbon Nanoemulsion for Inflammatory Macrophage Detection via PET and MRI

Running Title: Fluorocarbon Nanoemulsion for PET-MRI

Authors: Chao Wang¹, Benjamin I. Leach¹, Deanne Lister¹, Stephen R. Adams², Hongyan Xu¹, Carl Hoh¹, Patrick McConville^{1,3}, Jing Zhang⁴, Karen Messer⁴, Eric T. Ahrens¹

Affiliations:

¹Department of Radiology, University of California, San Diego, La Jolla, CA 92093 USA

²Department of Pharmacology, University of California, San Diego, La Jolla, CA 92093 USA

³In vivo, Inc., Boston, MA 02210 USA

⁴Moore's Cancer Center, University of California San Diego, La Jolla, CA 92093 USA

Keywords: fluorocarbon nanoemulsion, PET, MRI, fluorine-19, inflammation.

Corresponding Author:

Eric T. Ahrens

University of California, San Diego

9500 Gilman Dr. #0695

La Jolla, CA 92093-0695

Phone: (858) 246-0279

eta@ucsd.edu

First Author:

Chao Wang (Postdoctoral Scholar)

University of California, San Diego

9500 Gilman Dr. #0695

La Jolla, CA 92093-0695

Phone: (858) 534-9712

chw124@ucsd.edu

Word Count: ~6500

Financial Support: This research was supported by National Institutes of Health (grants R01-EB024015 & R01-CA139579) and the California Institute for Regenerative Medicine (grant LA1-C12-06919).

ABSTRACT

Inflammation is associated with a range of serious human conditions including autoimmune and cardiovascular diseases and cancer. The ability to image active inflammatory processes greatly enhances our ability to diagnose and treat these diseases at an early stage. We describe molecular compositions enabling sensitive and precise imaging of inflammatory hotspots *in vivo*.

Methods: Functionalized fluorocarbon nanoemulsion, with fluorourous-encapsulated radiometal chelate (FERM), serves as a platform for multimodal imaging probe development. The ^{19}F -containing FERM nanoemulsion encapsulates ^{89}Zr in the fluorourous oil, via fluorinated hydroxamic acid chelate. Simple mixing of radiometal with pre-formed aqueous nanoemulsion prior to use yields FERM, a stable *in vivo* cell tracer, enabling whole-body ^{89}Zr positron emission tomography (PET) and ^{19}F magnetic resonance imaging (^{19}F MRI) following a single intravenous injection.

Results: FERM nanoemulsion is intrinsically taken up by phagocytic immune cells, particularly macrophages, with high specificity. FERM stability is demonstrated by a high correlation between ^{19}F and ^{89}Zr content in blood (correlation coefficient > 0.99). Image sensitivity is observed in an acute infection rodent model at low dose (37 kBq). The versatility of FERM is further demonstrated in inflammatory bowel disease and 4T1 tumor models.

Conclusion: Multimodal detection using FERM yields robust whole-body lesion detection and leverages the strengths of combined PET/ ^{19}F MRI. FERM nanoemulsion production is scalable and potentially useful for precise diagnosis, stratification and treatment monitoring of inflammatory diseases.

Introduction

Inflammation is a defensive innate immune response toward invasive stimuli and features activation and recruitment of immune cells. Though it beneficially promotes pathogen clearance and tissue recovery, uncontrolled inflammatory responses drive disease pathobiology. While conventional tissue contrast-based imaging methods, including proton MRI and CT, detect non-cell-specific inflammation lesions at late stage, molecular imaging methods offer the potential for increased specificity, earlier diagnosis, and improved therapeutic outcomes. Thus, there is keen interest in developing molecular imaging probes with precise targeting to inflammatory cells and markers (1).

The PET probe (18)F-fluorodeoxyglucose (FDG) serves as an imaging biomarker for numerous inflammatory diseases. However, FDG can have prominent uptake in tissues such as heart, kidney and gastrointestinal tract that may confound image interpretation for diseases affecting these regions (2,3). In the case of solid tumor and metastasis, it is challenging to distinguish between tumor associated macrophages (TAMs) and tumor cells in FDG PET scans, as both are metabolically active and take up the agent. Other small molecule radiotracers targeting inflammatory markers, such as cytokines, translocator proteins, enzymes, and integrin receptors, have been designed for enhanced specificity with varying degrees of success (4,5). Nanoparticle PET tracers for macrophages have also been explored, including ^{18}F and ^{64}Cu polyglucose (6,7) and ^{89}Zr dextran (8).

The size and morphology of nanoemulsion droplets make them susceptible to endocytosis by phagocytic immune cells, providing a powerful cell delivery approach for efficient intracellular macrophage labeling *in situ*. Intravenously administered fluorocarbon nanoemulsions enable background-free 'hotspot' ^{19}F MRI detection (9). The nanoemulsion droplets are scavenged *in situ*

by cells of the reticuloendothelial system (RES), particularly monocytes, macrophages, but also neutrophils and dendritic cells (10). The fluororous droplets coalesce into phagocyte lysosomal vesicles and macropinosomes (11), thus escaping osmotic pressure based cell efflux (12) and yields durable labeling, in contrast to small molecule tracers (13). Fluorocarbons have a proven safety profile and a well-characterized biodistribution and pharmacokinetics. The biological inertness and gas-dissolving property of fluorocarbons have made them major candidates for oxygen-carrying blood substitutes (14) since the 1980s. Moreover, clinical immunotherapeutic cells, pre-labeled with fluorocarbon nanoemulsion, have been longitudinally imaged with ^{19}F MRI post-inoculation into cancer patients (15).

Here, we investigate novel compounds for sensitive and precise inflammation imaging using PET and ^{19}F MRI. We synthesized functionalized fluorocarbon nanoemulsions (~160 nm droplet size) to incorporate a fluororous-encapsulated radiometal chelate (FERM) that captures ^{89}Zr into the fluororous phase of the preformed nanoemulsion via a simple premix step (Fig.1A). ^{89}Zr has a relatively long half-life (3.3 days) matching the organ-retention time of many fluorocarbons used in biomedicine (e.g., perfluorooctylbromide, PFOB, half-life 5.1 d) (16); ^{89}Zr is widely used in clinical trials to label monoclonal antibodies for PET (17). The highly hydrophobic nature of fluorocarbons helps exclude competition from water, cations, lipids and proteins that may contribute to the dissociation of ^{89}Zr from the carrier. Nanoemulsions formulated with chelate have a long shelf-life, and radiolabeling prior to use minimizes radiation-intensive steps for potential clinical trial use.

Using FERM, we demonstrate effective detection of macrophage-associated inflammation using multimodal PET/ ^{19}F MRI in murine models of acute infection, inflammatory bowel disease (IBD) and breast cancer. Results display robust whole-body lesion detection that leverages the

strengths of PET (sensitivity), ^{19}F MRI (low background), and ^1H MRI and CT (high resolution anatomical localization). Overall, FERM nanoemulsion offers simplicity and highly specific targeting of phagocytic immune cells *in vivo*.

Materials and Methods

Details on the synthesis of fluorous hydroxamic acid (FHOA) and radiolabeled FERM nanoemulsion are provided in the Supplemental Information. All animal experiments followed protocols that were approved by University of California San Diego's Institutional Animal Care and Use Committee.

Blood Circulation Time and Agent Stability *in vivo*

The blood half-life of FERM nanoemulsion (perfluoro-15-crown-5-ether, PFCE) was monitored using γ -counting and ^{19}F nuclear magnetic resonance (NMR). The ^{89}Zr labeled FERM was injected into of C57BL6 mice (n=6, ~40 g, Jackson Laboratory, Bar Harbor, ME) via tail vein at an activity dose of 3.145 MBq (0.2 mL). Mice were anesthetized using 1-2% isoflurane in oxygen, and blood samples were collected from retro-orbital sinus using capillaries. A 100 μL blood sample was pipetted into to a 5 mm NMR tube, followed by the addition of lysis buffer (100 μL). The radioactivity of each sample was assayed and decay-corrected. After a 5-week ^{89}Zr decay, sodium trifluoroacetate reference (NaTFA, 25 mM) in D_2O (50 μL) was added to blood samples. ^{19}F NMR spectra were acquired to calculate the fluorine content in the blood samples. A bi-exponential decay model was used to calculate blood half-lives.

Carrageenan Acute Inflammation Model

λ -Carrageenan plant mucopolysaccharide (Sigma-Aldrich, St Louis, MO) was injected (2% in saline, 50 μ L) into the right paw of female CD1 mice (Envigo, Indianapolis, IN). Swelling of the paw was confirmed visually and by paw width caliper measurements. FERM nanoemulsion was injected (3700 to 37 kBq, 0.2 mL) through tail vein, and $^{19}\text{F}/^1\text{H}$ MRI, PET and CT images were acquired 24 h post-injection in isoflurane anesthetized mice.

IBD Model

IBD was induced in female C57BL/6 mice (n=9) by administration of 3% dextran sulfate sodium salt (DSS) in drinking water *ad libitum* for 7 days prior to nanoemulsion injection. Control mice (n=3) received normal water. Disease progression was monitored daily by body weight loss, stool score and hemocult score (Supplemental Fig. 1). ^{89}Zr labeled FERM nanoemulsion (3.7 MBq, 0.2 mL) was injected through tail vein, and $^{19}\text{F}/^1\text{H}$ MRI, PET and CT images were acquired 24 h post-injection.

4T1 Tumor Model

Luciferase-expressing 4T1-luc2 cells (CRL-2539-luc2, ATCC, Manassas, VA) were maintained in Roswell Park Memorial Institute Medium (RPMI) medium containing 10% fetal bovine serum and 8 $\mu\text{g}/\text{mL}$ Blasticidin. Cells (5×10^6) were suspended in 50 μL phosphate buffered saline containing 50% matrigel and inoculated into the fourth mammary fat pad of female Balb/c mice (Envigo).

Tumor volumes were measured by calipers, and mice were sorted into two groups (n=5 each) when tumors reached a volume of 200-350 mm^3 (2-week cohort) and 900-1200 mm^3 (5-week

cohort). The ^{89}Zr labeled FERM nanoemulsion was injected into mice via tail vein at a dose of 3.7 MBq (200 μL), and $^{19}\text{F}/^1\text{H}$ MRI, PET, CT and BLI images were acquired 24 h post-injection.

PET/CT Imaging

PET/CT data were acquired using Inveon (Siemens, Malvern, PA, USA) and G8 (SOFIE, Culver City, CA, USA) scanners. Animals were anesthetized using 1-2% isoflurane in oxygen and warmed using and heated pads to maintain body temperature throughout the procedure. PET data were acquired for 10 minutes approximately 24 hours after ^{89}Zr FERM injection.

MRI

MRI was performed using a Bruker BioSpec 11.7 T MRI system running ParaVision 6 software and a dual-tuned $^{19}\text{F}/^1\text{H}$ 38 mm volume coil (Bruker BioSpin, Billerica, MA). Mice were anesthetized using 1-2% isoflurane in oxygen, and body temperature was maintained throughout the procedure using heated air. ^{19}F images were acquired using a RARE (rapid acquisition with relaxation enhancement) sequence with repetition time (TR) 1 s, echo time (TE) 20 ms, RARE factor 8, 30 \times 45 mm field of view, matrix size of 32 \times 48, 2 mm thick coronal slices (12), 150 averages and 15 min scan time. Anatomical ^1H scans were acquired using a RARE sequence with TR=2 s, TE=20.5 ms, RARE factor = 8, 10 averages, 1 min scan time, 1 mm thick slices (24), and field of view and orientation identical to the ^{19}F images.

Image Quantification and Visualization

Image quantification was performed using VivoQuant software (Invicro, Boston, MA). PET data were calibrated using a phantom containing ^{89}Zr . Footpad signals were quantified by placing a

cylindrical ROI over the paws and integrating signals. For analysis of IBD models, bone and bone marrow signals were segmented by thresholding CT images. Coarse ROIs were placed over the liver and spleen and segmented by thresholding the PET signal from 3.7×10^{-7} to 7.4×10^{-6} kBq. A single ROI was then placed over the peritoneum for subsequent analysis. ^{19}F data were quantified from a phantom placed in the field of view. For each image, three ROIs each were placed in the phantom and background to determine signal values and errors. Histograms were produced using VivoQuant software, with ranges set from $0-1 \times 10^{-4}$ %ID per voxel for PET imaging and from 0 to 3×10^{24} F-atoms/mL for ^{19}F MRI. For clarity, beds and phantoms were masked by generating an ROI around the mouse by thresholding the CT image, then exporting as a separate image. For display purposes, PET and ^{19}F MRI were co-registered by applying a transformation derived from co-registration of CT and ^1H images using an affine or nonlinear transformation algorithm in VivoQuant, and images were rendered in pseudo-color.

Statistics

The two-sample unpaired t-test was used for significance analysis. A $p < 0.05$ was considered significant. Statistical software R (<http://www.r-project.org>) was used for blood sample pharmacokinetic analyses. The function “biexp” was used to build the biexponential model for estimation of two-phase half-lives for both gamma counting and ^{19}F NMR, and bootstrapping techniques were used to calculate 95% confidence intervals.

Results

Preparation and Characterization of FERM Nanoemulsion

To formulate FERM nanoemulsion, we synthesized FHOA for Zr^{4+} binding. FHOA was prepared at gram scale using an Aza-Michael reaction (18) between a fluororous acrylamide (FA) and primary diamine (Fig. 1B). FHOA shares the hydroxamic acid units of the hexadentate desferrioxamine (DFO), a commonly used Zr^{4+} chelator for immuno-PET (19). The FHOA chelate provides eight oxygen coordination sites to saturate the Zr^{4+} sphere to avoid labile binding with H_2O and biomolecules, which are speculated to be a source of Zr-DFO instability (20). Force field simulation (Molecular Mechanics 2, ChemDraw, PerkinElmer, Waltham, MA) shows the formation of a distorted square antiprismatic complex, with an averaged Zr-O length of 2.1 Å, close to the 2.2 Å calculated from the X-ray structure of Zr-tetrahydroxamate (21). FHOA has a fluorine content of 54.26 % and is soluble in PFOB up to 15 mM (at room temperature) and PFCE up to 2 mM with mild heating; both of these fluorocarbons have been used for ^{19}F MRI (9,22). Titration of $ZrCl_4$ (non-radioactive) into FHOA in solution causes attenuation and shifting of FHOA peaks in 1H and ^{19}F NMR (Supplemental Fig. 2); no peak change is observed beyond 1 eq, suggesting a 1:1 ratio for Zr-FHOA binding. Binding of FHOA to $ZrCl_4$ (1 eq) in solution is rapid, with completion in <20 min (Supplemental Fig. 3).

Among various biologically relevant metals, Fe^{3+} is the strongest competitor for Zr^{4+} chelate. Addition of Fe^{3+} to FHOA in nanoemulsion causes an increase in UV-Vis absorption at ~450 nm, which is then reduced by addition of Zr^{4+} , suggesting Fe^{3+} displacement by Zr^{4+} (Supplemental Fig. 2). Extinction of absorption at 450 nm was monitored and fitted, yielding bi-exponential decay half-lives of 0.32 ± 0.07 h and 2.91 ± 0.26 h. To further assess Fe^{3+} competition, we measured the change in the ^{19}F spin-lattice relaxation time (T_1) in the nanoemulsion upon metal

binding. Fe^{3+} added to FHOA in nanoemulsion caused a 53% drop in ^{19}F T_1 (from 1.2 s to 0.6 s) due to the paramagnetic relaxation enhancement mechanism (23). Subsequent addition of ZrCl_4 recovers T_1 to 0.96 s via the displacement of strongly paramagnetic Fe^{3+} with Zr^{4+} . Conversely, addition of excess Fe^{3+} to Zr-saturated nanoemulsion only decreases T_1 by 5.7%. These data indicate that Zr^{4+} forms a more stable complex with FHOA than Fe^{3+} .

The FHOA was fully dissolved in the fluorocarbons before formulating into aqueous FERM nanoemulsions, as described in the Supplemental Information, yielding mean diameters ~ 160 nm and polydispersity index < 0.1 (Supplemental Table 1). Inclusion of FHOA (1 or 10 mM) has no statistically significant impact ($p > 0.05$) on the nanoemulsion size or stability over at least two months. Cells labelled with FERM nanoemulsion show no significant cytotoxicity over 48 h (Supplemental Fig. 4).

Radiolabeling FERM Nanoemulsion

Preformed PFOB or PFCE nanoemulsions (1 mL) containing chelate, and formulated with lipid-based surfactants, were radiolabeled by mixing with $^{89}\text{ZrCl}_4$ (in 1 M HCl) at room temperature for 3 hours. Unbound ^{89}Zr was removed by a single gel filtration step, resulting in a radiochemical yield of $63.2 \pm 6.5\%$ in 0.8 mL elution. We also tested nanoemulsion radiolabeling using ^{89}Zr -oxalate (in 1 M oxalic acid), where unlike $^{89}\text{ZrCl}_4$, neutralization was necessary to achieve efficient labeling. Radiolabeling yield of FERM is $50.9 \pm 4.7\%$ ($\text{pH} = 6.5$) with ^{89}Zr -oxalate 3 h after labeling. As a substitute for lipid surfactant, efficient radiolabeling of nanoemulsion was also achieved with a triblock copolymer surfactant, Pluronic F68, with $^{89}\text{ZrCl}_4$ yields of $58 \pm 7.1\%$ for FERM. We collected only 0.8 mL elution to minimize unbound $^{89}\text{Zr}^{4+}$ impurity and dilution of fluorine concentration (which is undesirable for ^{19}F MRI). Overall, FERM nanoemulsion

radiolabeling is flexible with respect to surfactant type, as it relies on an encapsulated chelate in the inert fluorocarbon core.

***In vivo* FERM Nanoemulsion Blood Stability and Half-life**

Nanoemulsion circulation half-life and *in vivo* stability were investigated in wild-type mice. Animals received a single intravenous injection of FERM nanoemulsion (n=6, PFCE, 3.14 MBq, $\sim 6 \times 10^{20}$ F atoms) via the tail vein. Longitudinal blood samples over a 24 h period were assayed using both gamma dosimetry and ^{19}F NMR (Fig. 1C). The γ -count data is decay-corrected, and the total fluorine content in the samples is determined by quantitative ^{19}F NMR spectroscopy. We observe a strong correlation between the two methods (Pearson's coefficient 0.99), indicating a retention of ^{89}Zr in the ^{19}F containing nanoemulsion. The results demonstrate stability of the complex *in vivo* for >24 h. The time-course data in Fig. 1C display multiexponential behavior, and a two-compartment biexponential model was used to estimate the half-lives. Bootstrapping techniques (24) were used to calculate the median (interquartile range, IQR) and differences of half-lives at 95% confidence interval. For dosimetry, the analysis yields median (IQR) half-lives of 0.6 (0.2) h and 14.5 (0.07) h, respectively. The ^{19}F NMR method results in median half-lives of 0.90 (0.01) h and 14.6 (0.11) h, respectively. We attribute the fast phase to perfusion and dilution of agent in the blood stream, and the slow phase to the clearance of agent from blood by the RES, including uptake by monocytes and macrophages (25). The fast half-life was 11-78% higher measured by ^{19}F NMR compared to the dosimetry method. The difference in the slow phase decay between the two methods is less than 1% which is insignificant.

Visualizing Acute Inflammation *in vivo*

FERM nanoemulsion is a versatile preclinical inflammation agent for a wide range of diseases. We initially investigated the feasibility of PET/¹⁹F MRI inflammation detection in an acute inflammation rodent model. The model uses an injection of λ -carrageenan plant mucopolysaccharide into the footpad of mice and is commonly used to test anti-inflammatory drugs and immune response (26). ⁸⁹Zr-labeled FERM nanoemulsion was injected (n=3, 3.7 MBq, $\sim 6 \times 10^{20}$ F atoms) by tail vein 1 h after carrageenan treatment. PET/CT images were acquired 24 h thereafter to permit FERM uptake by the RES, including macrophages. In PET, mice receiving FERM, formulated with either PFOB or PFCE, display hotspots in the inflamed right paw, with little observable signal on the contralateral side (Fig. 2A). Prominent signals are also observed in spleen and liver. Immunohistochemical results in the hind paws show macrophage fluorocarbon uptake *in situ* following intravenous infusion (Supplemental Fig. 5), consistent with prior studies in various inflammation models (9,27). Control animals receive either free ⁸⁹ZrCl₄ or ⁸⁹Zr treated nanoemulsion without chelate, and both display similar trafficking patterns (Fig. 2A & Supplemental Fig. 6); free ⁸⁹Zr is taken up by bone (28).

We performed region of interest (ROI) analysis of the footpad PET signals. In FERM injected animals (PFOB, 3.7 MBq), uptake in the right (inflamed) hind paw is 3.8 ± 1.0 % of injected dose (%ID), compared to 0.34 ± 0.08 %ID in the left (control) hind paw. Mice were euthanized, and gamma counting of excised hind paws confirm differential uptake (Fig. 2B), with the right paw showing approximately 7-fold higher uptake than the left (23.3 ± 11.9 %ID/g versus 3.4 ± 0.56 %ID/g, respectively, n=3). The bulk of the nanoemulsion was detected by dosimetry in liver (14.2 ± 2.9 %ID/g) and spleen (58.2 ± 2.9 %ID/g). In animals injected with lipid-associated ⁸⁹Zr PFOB nanoemulsion without chelate (3.7 MBq, n=3), uptake was 0.11 ± 0.01 %ID/g and

0.05% \pm 0.01 %ID/g in the right and left paws, respectively. For the lipid-associated ^{89}Zr PFOB nanoemulsion, the bulk of the activity was found in the bone and minimally detected in liver and spleen, as is seen for free ^{89}Zr (Supplemental Fig. 6).

A single dose of FERM nanoemulsion enables multimodal ^{19}F MRI and PET detection in the same subject. In the acute inflammation model, *in vivo* spin density-weighted ^{19}F and T_2 -weighted ^1H multi-slice images were acquired, followed by PET/CT scans in the same mice. Both ^{19}F MRI and ^{89}Zr PET scans display colocalized hotspots in the inflamed right paw and minimal signals in the contralateral paw. Quantification of both ^{19}F and ^{89}Zr hotspots in right paw display >10-fold higher signal compared to contralateral paw (Fig. 2C).

To evaluate *in vivo* PET detection at clinically relevant activity doses, we performed descending dose tests (3700 to 37 kBq) for injected FERM nanoemulsion in the acute inflammation model (Fig. 2D). In clinical trials using ^{89}Zr immuno-PET imaging, acceptable patient injection doses range from approximately 37 to 203.5 MBq, equivalent to 0.74 to 3.33 kBq per gram body weight (assuming 60 kg/human) (17). For mice (~30 g), the corresponding clinical equivalent doses range from approximately 18.5 to 103.6 kBq. At all doses used the ratio of uptake values in the right (inflamed) versus left (normal) paw is maintained at ~10 with statistical significance ($p < 0.05$, $n = 3$, Fig. 2D). At the lower doses, the inflammation foci remain as the dominant image hotspot, thus showing inflammation specificity. At 37 kBq level, the inflammation site remains clearly visible with a 10 min PET scan time. This translates to a human dose of 4 mL FERM (18.5 MBq/mL) comprising ~0.8 g of fluorocarbon, a level that is an order of magnitude lower than historical artificial blood substitute doses (16). Overall, at clinically relevant activity doses the inflammation diagnostic potential of FERM nanoemulsion appears to be maintained.

Visualizing IBD

Next, we explored the use of FERM for imaging IBD in a mouse model using PET/¹⁹F MRI. The IBD model was induced by adding DSS to drinking water for C57BL/6 mice, resulting in ulcerative colitis-like inflammation, with prominent inflammatory infiltrates, including macrophages in the gastrointestinal tract (29). IBD clinical symptoms peak at approximately eight days after the start of DSS treatment. At peak, a single intravenous injection of ⁸⁹Zr FERM nanoemulsion (n=5, 0.2 mL, 3.7 MBq, ~6×10²⁰ F atoms) was administered, and 24 h thereafter ⁸⁹Zr PET/CT and ¹⁹F/¹H MRI data were acquired. Representative images are shown Fig. 3, where both the PET and ¹⁹F MRI data are co-registered to CT. Major hotspots are observed in the colon in ⁸⁹Zr PET images for all IBD mice. IBD lesions are patchy and heterogenous among subjects (30) and distributed in ascending and descending colon. Control mice, without DSS induction, display prominent uptake in liver and spleen with minimal colon signal, as expected for RES clearance of FERM nanoemulsion. ¹⁹F MRI in the same animals also display inflammatory hotspots in colon (Fig. 3B). Generally, ¹⁹F MRI lesion signals are more punctate compared to the relatively diffuse PET signals. Overlays of ¹⁹F and high-resolution ¹H anatomical images show ¹⁹F signal localization in the anatomical context of the colon wall (Fig. 3C). To quantitate inflammation in bowel, ROIs were placed around peritonea, and the resulting signal histograms for PET and ¹⁹F MRI are calculated (Supplemental Fig. 7). Both methods clearly show a much larger proportion of high-signal voxels in the IBD mice in comparison to controls. Notably, the anatomical signal patterns for PET and ¹⁹F MRI are largely overlapping (Fig. 3D).

Visualizing TAMs

TAMs play a central role in the initiation, progression and metastasis of tumors, and their density in the tumor microenvironment is often associated with tumor aggressiveness and patient survival rate (31). Imaging TAMs and metastasis-associated macrophages may enable early malignancy detection, as well as response assessment of immunotherapies. We investigated the use of FERM nanoemulsion for PET/¹⁹F MRI macrophage imaging in a breast cancer mouse model (Fig. 4). Tumor cells (4T1) expressing luciferase were implanted in mammary fat pad, and bioluminescence imaging (BLI) confirmed primary tumor growth in flank. FERM nanoemulsion PET/¹⁹F MRI scans were conducted at 2 weeks (“early”, n=5) or 5 weeks (“late”, n=5) post-implantation in separate cohorts. At 24 h prior to imaging, animals received intravenous ⁸⁹Zr FERM nanoemulsion (3.7 MBq, ~6×10²⁰ F atoms). In the early cohort, PET images (Fig. 4A) display major hotspots in the whole tumor area, as well as in the liver and spleen. In the late group, FERM has significant presence in the flank tumor periphery for both PET and ¹⁹F MRI (Fig. 4B, C), with minimal signal in the tumor center, consistent with peripheral macrophage infiltration and tumor core necrosis. Gamma counting of the excised tumors confirm high tumor uptake of the agent, with 5.3 ± 1.8 %ID in early tumors and 10.7 ± 3.6 %ID in late tumors. Notably, putative metastases are observed in the axillary lymph node region, visible with both PET and BLI (Fig. 4B), in 2 out of 5 animals in the late cohort. In the late cohort lungs, we observe slightly elevated, diffuse PET signal (n=5), which was not apparent in ¹⁹F MRI or BLI.

Discussion

We describe the development of ⁸⁹Zr FERM nanoemulsion for imaging inflammatory disease with high specificity, sensitivity and versatility, using both PET and ¹⁹F MRI. We devised a fluoros

^{89}Zr chelator FHOA that effectively encapsulates the radioisotope into the nanoemulsion core. This strategy minimizes radioisotope leakage and non-specific cell labeling. FHOA was prepared and purified at gram scale in a single run. FERM is formulated as a cold nanoemulsion, preloaded with chelate, and displays long term stability (>2 months). Before intravenous delivery, FERM is radiolabeled with ^{89}Zr via simple premix and filtration steps. The use of ^{89}Zr with its relatively long half-life (3.3 d) allows for RES cell (macrophage) uptake of nanoemulsion, as well as longitudinal studies over several days with a single administration.

In vivo stability of FERM nanoemulsion was evaluated by blood pharmacokinetic analysis and suggests minimal dissociation *in vivo*. Both dosimetry and ^{19}F NMR intensity analyses of serial blood samples display bi-exponential decreases over time; the slow time constant (~15 h), presumed to be RES uptake, and overall shows good agreement between the two measurement methods (>0.99 correlation). Thus, the ^{89}Zr and ^{19}F signal generators stay co-complexed during the RES uptake period. The fast-phase time constant, representing the initial blood perfusion of agent, varies when measured by dosimetry ($t_{1/2}$ =36 min) and ^{19}F ($t_{1/2}$ =54 min, $p < 0.05$). Variations in the timing of blood sample γ -counting (~1-4 min), imperfect gel-filtration purification, or residual ^{89}Zr bound to lipid headgroups (32) of the surfactant, all could potentially lead to measurement discrepancies in the fast time constant.

Prior preclinical studies have used ^{19}F MRI with fluorocarbons for macrophage labeling *in situ*, for example in myocarditis (9), solid organ transplant rejection (33), IBD (27,34), as well as various cancer models (35-37). Importantly, these same studies firmly establish intracellular tissue macrophage uptake of fluorocarbon agent as the dominate image signal observed *in vivo*. For example, IBD studies have shown exclusive colocalization of fluorescently-conjugated fluorocarbon nanoemulsion and F4/80+ macrophage in immunohistochemistry micrographs, as

well as correlation between histopathology quantification of lesion burden in colon wall to total ^{19}F signal in the same specimens (34). Additionally, quantitative PCR analysis correlating macrophage burden via CD68 RNA levels with ^{19}F signal in colon samples show a linear relationship (27). Moreover, clodronate liposome treatment ablates the ^{19}F signals in the colon of IBD mice (27). In solid tumor models, immunohistochemistry shows specific uptake of fluorescent fluorocarbon nanoemulsion in macrophages both at primary tumor periphery at late stages and at metastasis sites (35-38). While fluorocarbon nanoemulsions have been widely studied for ^{19}F MRI, its description for use as a PET tracer has been very limited (39,40).

The FERM nanoemulsion shows promise for precise detection of a broad range of inflammatory lesions with high macrophage specificity. In the case of IBD, and macrophages derived from blood monocytes are important mediators of chronic inflammation in IBD along with Th1 and Th2 type T cells (41,42). The ‘gold-standard’ IBD test is colonoscopic biopsy, an invasive procedure requiring multiple tissue bites for diagnosis, which may result in sampling errors and cause patient discomfort, thus driving the need for more precise diagnostics for staging and monitoring treatment course. Physiologic bowel uptake of ^{18}F -FDG is highly variable in the colon and can be quite intense, especially in patients on Metformin (43), thus limiting FDG’s usefulness. Oncology also presents another major area of use for FERM for precision macrophage imaging due to the diagnostic potential, as well as the increasing focus on macrophages as therapeutic targets (44).

In both PET and ^{19}F MRI, lesion foci are the only major hotspots other than the liver and spleen. Hotspots display anatomical similarities across both modalities, indicative of FERM stability *in vivo*. The MRI-apparent lesions appear as more punctate compared to the more diffuse PET detected lesions. There are fundamental differences between the two imaging techniques with

regards to intrinsic sensitivity and resolution, image reconstruction methods, point-spread functions, and partial-volume effects that impact quantification and small lesion appearance (45,46). A more concrete understanding of the interplay among these factors could be achieved by mathematical modeling in future studies. Generally, ^{19}F MRI is prone to false negative signals due to sensitivity limitations, whereas high-sensitivity PET imaging is prone to false positives, thus a bimodal readout could potentially provide a complementary representation of the ground-truth lesion macrophage distribution using FERM nanoemulsion. As a practical matter, the ^{19}F is advantageous as a stable tag to assay nanoemulsion biodistribution via ^{19}F NMR of tissue samples (47), as well as the fate of the ^{89}Zr +fluorocarbon complex when combined with g-counting (*e.g.*, Fig. 1C).

While we acquired PET and ^{19}F MRI using separate instruments, future advancements in imaging hardware may be feasible to enable simultaneous acquisition of PET/ ^{19}F MRI data. Recently, dual-mode PET and ^1H -only MRI scanners have been in clinical service, for example, in cardiology, oncology and neurology (48). Whole-body clinical PET to identify putative lesions, followed by inflammation hotspot $^{19}\text{F}/^1\text{H}$ MRI in a smaller field of view with high soft-tissue resolution, may yield a rich dataset for treatment planning and response monitoring.

Although the safety and detectability assessments for FERM nanoemulsion are preliminary, the results suggest translational potential in a broad range of inflammatory disease types. One of the challenges with ^{19}F MRI is that capabilities for ‘X-nuclei’ imaging is uncommon in a clinical setting compared to PET, thus initial use will likely involve PET-only readouts. The scalable production of FERM nanoemulsion, together with streamlined radiolabeling, may enable practical implementation in a clinical setting.

Conclusions

FERM nanoemulsion is shown to be effective for imaging macrophage-associated inflammatory disease using PET and ^{19}F MRI and shows versatility in a range of preclinical models. The novel fluorine ^{89}Zr chelator FHOA encapsulates the radioisotope into the nanoemulsion core which minimizes radioisotope leakage and non-specific cell labeling. FERM nanoemulsion may open-up new avenues for precise stratification, diagnosis and treatment monitoring in cases where normal physiologic uptake of ^{18}F -FDG may obscure the cellular inflammatory component of disease.

Figures

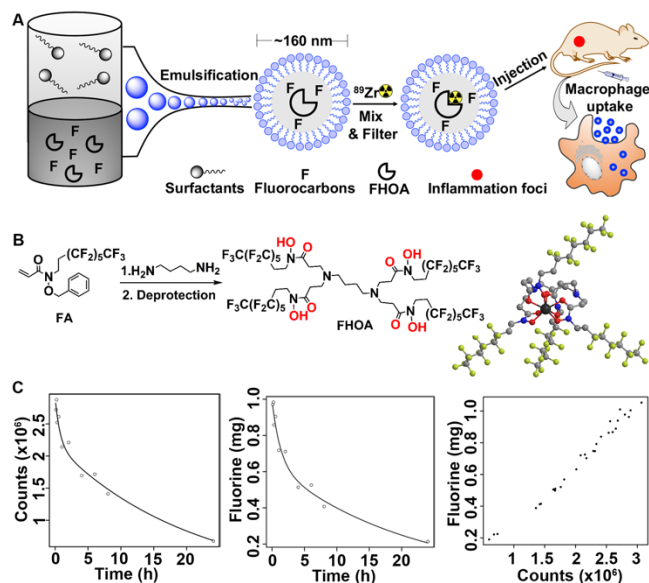


Figure 1. Preparation and pharmacokinetic analysis of FERM nanoemulsion. In (A), the experimental workflow is shown. (B) Displays the chemical structure of FHOA and its simulated complex with Zr^{4+} (black = Zr, red = O, blue = N, grey = C, yellow = F, H omitted). Panel (C) displays pharmacokinetic analysis of FERM nanoemulsion (PFCE) in mouse as measured by decay-corrected gamma counts and fluorine content in blood samples ($100 \mu\text{L}$, $n=3$ mice per time point) drawn over a 24 h period. Bi-exponential fits are used to calculate decay half-lives. A scatterplot correlating gamma counts and fluorine content is shown (the Pearson correlation coefficient $r=0.9933$).

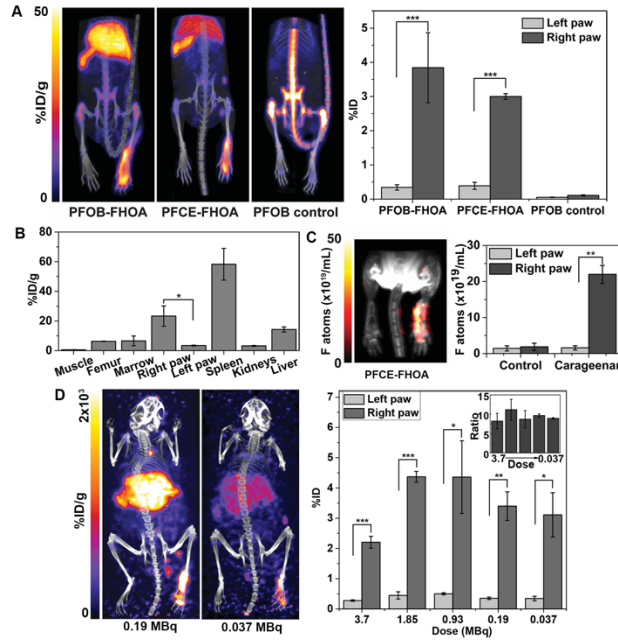


Figure 2. Visualization of acute footpad inflammation via *in situ* labeling of phagocytic immune cells with ^{89}Zr labeled FERM nanoemulsion. (A) Displays representative PET/CT in mice 24 h after intravenous injection of FERM nanoemulsion or control nanoemulsion without FHOA (left) and ROI results of PET signal in paws (right). (B) Shows biodistribution of FERM nanoemulsion in excised tissues measured by γ -counting post-imaging. (C) Displays composite $^{19}\text{F}/^1\text{H}$ MRI (left) from the mouse in (A) and quantification of fluorine content in footpads with and without carrageenan treatment. (D) Shows representative PET/CT of mice injected with low doses of FERM nanoemulsion (left) and ROI results of PET signals in paws (right); the inset shows the signal ratio of the right and left paws ($R: L$). Data are shown as mean \pm s.e.m. ($n=3$), where * denotes $P<0.05$, ** is $P<0.005$ and *** is $P<0.001$ in unpaired t-tests.

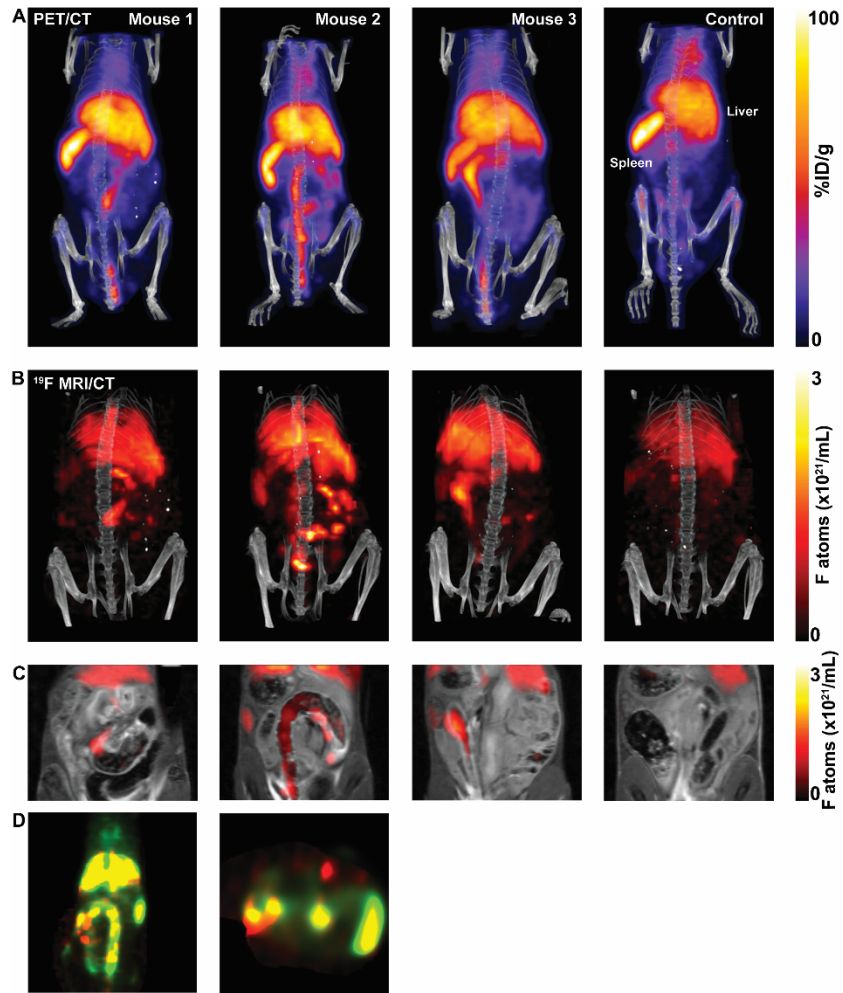


Figure 3. Multimodal PET/¹⁹F MRI in IBD mice. Panel (A) displays PET/CT images of three IBD mice and control (naïve) mice 24 h after intravenous injection of FERM nanoemulsion (3.7 MBq). (B) Shows composite ¹⁹F MRI/CT images of the mice in (A). Panel (C) are overlaid ¹⁹F MRI and ¹H MRI slices in the mouse from (B). In (D) we display composite PET and ¹⁹F MRI slices of coronal (left) and transverse (right) views, respectively. Here, ¹⁹F MRI=red, PET=green, and overlap=yellow.

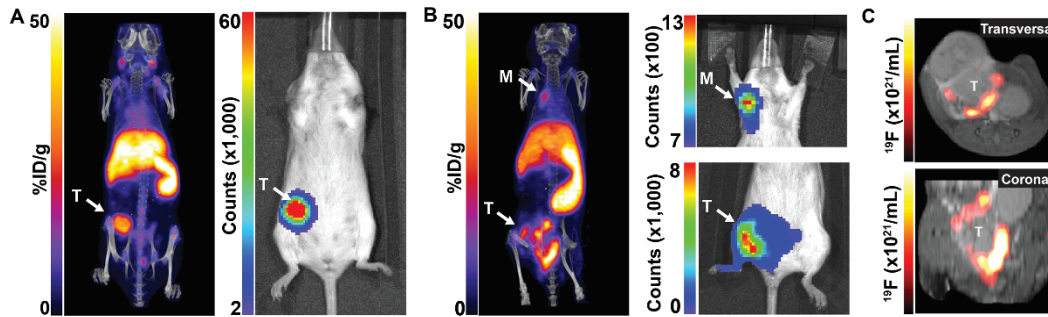


Figure 4. *In vivo* detection of TAMs and metastasis in 4T1 tumors using FERM nanoemulsion. Panels A and B show representative PET/CT (left) and BLI images (right) of mice 2 and 5 weeks post-implantation, respectively, with 4T1 breast cancer cells (T=tumor, M= metastasis). BLI of metastasis in 5-week group (B, right) is acquired after shielding the primary tumor. Panel (C) are overlaid $^{19}\text{F}/^1\text{H}$ MRI slices at tumor site from the same mouse as (B) and shows hotspots in tumor periphery consistent with TAM localization. The metastasis is outside the image field of view.

Disclosure

E.T.A. is a founder and shareholder of Celsense, Inc. No other potential conflicts of interest relevant to this article exist.

Key Points

Question: Can we use nanoemulsions with fluorocarbon-encapsulated radiometal for multimodal PET and ^{19}F MRI of inflammatory macrophages?

Pertinent Findings: Fluorous-encapsulated ^{89}Zr nanoemulsion is readily complexed prior to use and stable *in vivo*. Following intravenous injection we demonstrate multimodal imaging of inflammatory hotspots with high specificity in acute inflammation, IBD and solid tumor rodent models.

Implications for Patient Care: The ^{89}Zr nanoemulsion technology may provide a new approach for precise stratification, diagnosis and treatment monitoring for a range of inflammatory diseases.

References

1. Hammoud DA. Molecular imaging of inflammation: current status. *J Nucl Med.* 2016;57:1161-1165.
2. Rosenbaum SJ, Lind T, Antoch G, Bockisch A. False-positive FDG PET uptake--the role of PET/CT. *Eur Radiol.* 2006;16:1054-1065.
3. Hamidizadeh R, Eftekhari A, Wiley EA, Wilson D, Alden T, Bénard F. Metformin discontinuation prior to FDG PET/CT: A randomized controlled study to compare 24- and 48-hour bowel activity. *Radiology.* 2018;289:418-425.
4. Tahara N, Mukherjee J, de Haas HJ, et al. 2-Deoxy-2-[¹⁸F]fluoro-D-mannose positron emission tomography imaging in atherosclerosis. *Nat Med.* 2014;20:215-219.
5. Wu C, Li F, Niu G, Chen X. PET imaging of inflammation biomarkers. *Theranostics.* 2013;3:448-466.
6. Keliher EJ, Ye YX, Wojtkiewicz GR, et al. Polyglucose nanoparticles with renal elimination and macrophage avidity facilitate PET imaging in ischaemic heart disease. *Nat Commun.* 2017;8:14064-14076.
7. Kim HY, Li R, Ng TSC, et al. Quantitative imaging of tumor-associated macrophages and their response to therapy using ⁶⁴Cu-labeled Macrin. *ACS Nano.* 2018;12:12015-12029.
8. Keliher EJ, Yoo J, Nahrendorf M, et al. ⁸⁹Zr-labeled dextran nanoparticles allow in vivo macrophage imaging. *Bioconjug Chem.* 2011;22:2383-2389.
9. Flögel U, Ding Z, Hardung H, et al. In vivo monitoring of inflammation after cardiac and cerebral ischemia by fluorine magnetic resonance imaging. *Circulation.* 2008;118:140-148.
10. Temme S, Bonner F, Schrader J, Flögel U. ¹⁹F magnetic resonance imaging of endogenous macrophages in inflammation. *Wiley Interdiscip Rev Nanomed Nanobiotechnol.* 2012;4:329-343.
11. Ahrens ET, Flores R, Xu H, Morel PA. In vivo imaging platform for tracking immunotherapeutic cells. *Nat Biotechnol.* 2005;23:983-987.
12. Isaacks RE, Bender AS, Kim CY, Shi YF, Norenberg MD. Effect of osmolality and anion channel inhibitors on myo-inositol efflux in cultured astrocytes. *J Neurosci Res.* 1999;57:866-871.
13. Fairclough M, Prenant C, Ellis B, et al. A new technique for the radiolabelling of mixed leukocytes with zirconium-89 for inflammation imaging with positron emission tomography. *J Labelled Comp Radiopharm.* 2016;59:270-276.
14. Squires JE. Artificial blood. *Science.* 2002;295:1002-1005.

15. Ahrens E, Helfer, BM, O'Hanlon, CF, Schirda, C. Clinical cell therapy imaging using a perfluorocarbon tracer and fluorine-19 MRI. *Magn Reson Med*. 2014;72:1696-1701.
16. Riess JG. Understanding the fundamentals of perfluorocarbons and perfluorocarbon emulsions relevant to in vivo oxygen delivery. *Artif Cell Blood Sub*. 2005;33:47-63.
17. Jauw YW, Menke-van der Houven van Oordt CW, Hoekstra OS, et al. Immuno-positron emission tomography with zirconium-89-labeled monoclonal antibodies in oncology: what can we learn from initial clinical trials? *Front Pharmacol*. 2016;7:131.
18. Koshti N, Reddy GV, Jacobs H, Gopalan A. Convenient synthetic methods for the preparation of N-fluoroalkylhydroxamic acids. *Synth Commun*. 2002;32:3779-3790.
19. Deri MA, Zeglis BM, Francesconi LC, Lewis JS. PET imaging with ^{89}Zr : from radiochemistry to the clinic. *Nucl Med Biol*. 2013;40:3-14.
20. Patra M, Bauman A, Mari C, et al. An octadentate bifunctional chelating agent for the development of stable zirconium-89 based molecular imaging probes. *Chem Commun*. 2014;50:11523-11525.
21. Guerard F, Lee YS, Tripier R, Szajek LP, Deschamps JR, Brechbiel MW. Investigation of Zr(IV) and ^{89}Zr (IV) complexation with hydroxamates: progress towards designing a better chelator than desferrioxamine B for immuno-PET imaging. *Chem Commun*. 2013;49:1002-1004.
22. Rothe M, Jahn A, Weiss K, et al. In vivo ^{19}F MR inflammation imaging after myocardial infarction in a large animal model at 3T. *Magn Reson Mater Phy*. 2019;32:5-13.
23. Kislukhin AA, Xu H, Adams SR, Narsinh KH, Tsien RY, Ahrens ET. Paramagnetic fluorinated nanoemulsions for sensitive cellular fluorine-19 magnetic resonance imaging. *Nat Mater*. 2016;15:662.
24. Efron B, Tibshirani RJ. *An Introduction to the Bootstrap*. 1 ed. Boca Raton: Chapman and Hall/CRC Press; 1994.
25. Neubauer AM, Sim H, Winter PM, et al. Nanoparticle pharmacokinetic profiling in vivo using magnetic resonance imaging. *Magn Reson Med*. 2008;60:1353-1361.
26. Posadas I, Bucci M, Roviezzo F, et al. Carrageenan-induced mouse paw oedema is biphasic, age-weight dependent and displays differential nitric oxide cyclooxygenase-2 expression. *Br J Pharmacol*. 2004;142:331-338.
27. Kadayakkara DK, Ranganathan S, Young WB, Ahrens ET. Assaying macrophage activity in a murine model of inflammatory bowel disease using fluorine-19 MRI. *Lab Invest*. 2012;92:636-645.

28. Abou DS, Ku T, Smith-Jones PM. In vivo biodistribution and accumulation of ^{89}Zr in mice. *Nucl Med Biol.* 2011;38:675-681.
29. Na YR, Stakenborg M, Seok SH, Matteoli G. Macrophages in intestinal inflammation and resolution: a potential therapeutic target in IBD. *Nat Rev Gastroenterol Hepatol.* 2019;16:531-543.
30. Cho JH, Feldman M. Heterogeneity of autoimmune diseases: pathophysiologic insights from genetics and implications for new therapies. *Nat Med.* 2015;21:730-738.
31. Qian BZ, Pollard JW. Macrophage diversity enhances tumor progression and metastasis. *Cell.* 2010;141:39-51.
32. Abou DS, Thorek DL, Ramos NN, et al. ^{89}Zr -labeled paramagnetic octreotide-liposomes for PET-MR imaging of cancer. *Pharm Res.* 2013;30:878-888.
33. Hitchens TK, Ye Q, Eytan DF, Janjic JM, Ahrens ET, Ho C. F-19 MRI detection of acute allograft rejection with in vivo perfluorocarbon labeling of immune cells. *Magn Reson Med.* 2011;65:1145-1154.
34. Shin SH, Kadayakkara DK, Bulte JW. In Vivo ^{19}F MR imaging cell tracking of inflammatory macrophages and site-specific development of colitis-associated dysplasia. *Radiology.* 2017;282:194-201.
35. Khurana A, Chapelin F, Xu H, et al. Visualization of macrophage recruitment in head and neck carcinoma model using fluorine-19 magnetic resonance imaging. *Magn Reson Med.* 2018;79:1972-1980.
36. Makela AV, Gaudet JM, Foster PJ. Quantifying tumor associated macrophages in breast cancer: a comparison of iron and fluorine-based MRI cell tracking. *Sci Rep.* 2017;7:42109.
37. Makela AV, Foster PJ. Imaging macrophage distribution and density in mammary tumors and lung metastases using fluorine-19 MRI cell tracking. *Magn Reson Med.* 2018;80:1138-1147.
38. Balducci A, Wen Y, Zhang Y, et al. A novel probe for the non-invasive detection of tumor-associated inflammation. *Oncoimmunology.* 2013;2:e23034.
39. Fabiilli ML, Piert MR, Koeppe RA, Sherman PS, Quesada CA, Kripfgans OD. Assessment of the biodistribution of an [^{18}F]FDG-loaded perfluorocarbon double emulsion using dynamic micro-PET in rats. *Contrast Media Mol Imaging.* 2013;8:366-374.
40. Amir N, Green D, Kent J, et al. ^{18}F -Labeled perfluorocarbon droplets for positron emission tomography imaging. *Nucl Med Bio.* 2017;54:27-33.
41. Sheikh SZ, Plevy SE. The role of the macrophage in sentinel responses in intestinal immunity. *Curr Opin Gastroenterol.* 2010;26:578-582.

42. Mahida YR. The key role of macrophages in the immunopathogenesis of inflammatory bowel disease. *Inflamm Bowel Dis*. 2000;6:21-33.
43. Gontier E, Fourme E, Wartski M, et al. High and typical ^{18}F -FDG bowel uptake in patients treated with metformin. *Eur J Nucl Med Mol Imaging*. 2008;35:95-99.
44. Mantovani A, Marchesi F, Malesci A, Laghi L, Allavena P. Tumour-associated macrophages as treatment targets in oncology. *Nat Rev Clin Oncol*. 2017;14:399-416.
45. Rahmim A, Qi J, Sossi V. Resolution modeling in PET imaging: theory, practice, benefits, and pitfalls. *Med Phys*. 2013;40:064301.
46. Robson MD, Gore JC, Constable RT. Measurement of the point spread function in MRI using constant time imaging. *Magn Reson Med*. 1997;38:733-740.
47. Ahrens ET, Young W-B, Xu H, Pusateri LK. Rapid quantification of inflammation in tissue samples using perfluorocarbon emulsion and fluorine-19 nuclear magnetic resonance. *Biotechniques*. 2011;50:229-234.
48. Broski SM, Goenka AH, Kemp BJ, Johnson GB. Clinical PET/MRI: 2018 Update. *Am J Roentgenol*. 2018;211:295-313.

Detailed Synthesis of Fluorous Hydroxamic Acid (FHOA)

Except where noted, chemicals were purchased from Sigma-Aldrich (St. Louis, MO) or TCI America (Portland, OR), and solvents were purchased from Thermo Fisher Scientific (Pittsburgh, PA) and used as received. Fluorous solvents were purchased from Exflour Research Corporation (Round Rock, TX). Zirconium-89 (148-185 MBq in 1 M HCl or oxalic acid) was purchased from the University of Wisconsin-Madison. All handling and disposal of radioactive materials met local and Federal regulations.

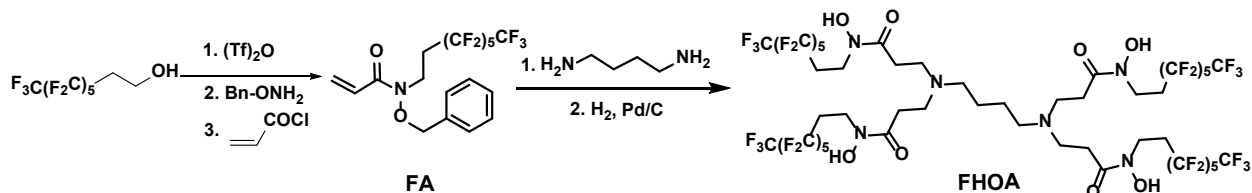
All synthetic reactions were carried out under N₂ unless otherwise noted. Reactions were monitored by thin layer chromatography and LC-MS (Ion Trap XCT with 1100 LC, Agilent, Santa Clara, CA) using an analytical Luna C18(2) reverse-phase column (Phenomenex, Torrance, CA), MeCN/H₂O (with 0.05% v/v CF₃CO₂H) linear gradients, 1 mL/min flow, and ESI positive or negative ion mode.

Compounds were purified by pre-packed silica gel columns on a CombiFlash automated system (Lincoln, NE, USA) equipped with a UV-Vis detector.

High-resolution mass spectrometry (HRMS) was performed by the Molecular Mass Spectrometry Facility at the University of California San Diego. UV-Vis absorption spectra were recorded on a Shimadzu UV-2700 (Kyoto, Japan) spectrophotometer. Nanoemulsion size and polydispersity was measured by dynamic light scattering (DLS) on a Malvern Zetasizer ZS (Malvern, PA). Solution NMR measurements were performed on a 9.4 Tesla spectrometer (AVANCE III HD-NanoBay, Bruker, Billerica, MA).

The starting material **FA** was prepared in ~5 g scale as colorless oil using fluorous alcohol as a starting material based on published methods (18) and confirmed by LC-MS (10-100% CH₃CN/H₂O for 20 min then 100% CH₃CN for 5 min, *t*=23.4 min, [M+H]⁺ measured 522.9,

calculated 523.1). ^1H NMR (400 MHz, CDCl_3) δ 7.43–7.36 (m, 5H), 6.70 (dd, $J = 17.1, 10.4$ Hz, 1H), 6.44 (dd, $J = 17.2, 1.9$ Hz, 1H), 5.77 (dd, $J = 10.3, 1.9$ Hz, 1H), 4.86 (s, 2H), 3.92 (t, $J = 8.0$ Hz, 2H), 2.44 (tt, $J = 17.9, 7.7$ Hz, 2H). ^{19}F NMR (376 MHz, CDCl_3) δ -80.77 (t, $J = 10.62$ Hz, 3F), -113.98–-114.40 (m, 2F), -121.88 (s, 2F), -122.85 (s, 2F), -123.05–-123.91 (m, 2F), -126.00–-126.29 (m, 2F).



A mixture of compound **FA** (4.88 mmol, 2.55 g) and 1,4-diaminobutane (1.08 mmol, 108.8 μL , Sigma-Aldrich) in acetonitrile (50 mL) were refluxed under N_2 for 72 hours to obtain the benzoyl-protected precursor **FHOA-OBn**. LC-MS showed **FHOA-OBn** to be the major product (10-100% $\text{MeCN}/\text{H}_2\text{O}$ for 20min then 100% CH_3CN for 5 min, $t=23.7$ min, $[\text{M}+\text{H}]^+$ measured 2179.8, calculated 2180.4). After the reaction cooled to room temperature, the solvent was evaporated, and the residue was re-dissolved in ethyl acetate (3 mL). The crude product was purified using a silica gel column (40 g) and eluted with $\text{CH}_3\text{OH}/\text{CH}_2\text{Cl}_2$ (0-8%, 15 min, linear gradient). A major peak centered at 11.5 min was collected and identified as **FHOA-OBn** by LC-MS. Solvents were evaporated, leaving **FHOA-OBn** as a colorless oil with a yield of $61\pm 6\%$ (1.44 g, $n = 3$). HRMS (m/z , ESI-TOF) for $[\text{M}+2\text{H}]^{2+}$ was calculated to be 1091.2207 and 1091.2198 was measured. ^1H NMR (400 MHz, CDCl_3) δ 7.37 (s, 20H, $-\text{C}_6\text{H}_5$), 4.82 (s, $-\text{OCH}_2\text{Ph}$, 8H), 3.82 (t, $J = 7.6$ Hz, 8H), 2.73 (t, $J = 7.3$ Hz, 8H), 2.52 (t, $J = 7.1$ Hz, 8H), 2.47–2.19 (m, 12H), 1.74 (s, 4H). ^{19}F NMR (376 MHz, CDCl_3) δ -80.83 (t, $J = 8.99$ Hz, $-\text{CF}_3$, 12F), -114.30 (p, $J = 18.4$ Hz, $-\text{CH}_2\text{CF}_2$, 8F), -121.97 (q, $J = 14.2$ Hz, 8F), -122.95 (s, 8F), -123.50 (t, $J = 13.8$ Hz, 8F), -126.10–-126.30 (m, 8F). ^{13}C NMR (101 MHz, CDCl_3) δ 174.71 ($\text{C}=\text{O}$), 134.16, 129.37, 129.23, 128.84,

127.15-99.89 (m, -CF₂-, weak), 54.03, 48.38, 38.48, 29.97, 29.73, 27.87 (t, -CH₂CF₂-, *J*=22.03 Hz), 24.96.

The **FHOA-OBn** (1.44 g) obtained was dissolved in ethanol (60 mL), then Pd/C (10%, 120 mg) was added. The mixture was stirred at room temperature under 1 atm H₂ for 16 h. LC-MS confirmed the disappearance of FHOA-OBn and formation of FHOA (10-100% CH₃CN/H₂O for 20 min then 100% CH₃CN for 5 min, *t*=22.6 min, [M+H]⁺ measured 1819.5, calculated 1820.2). The mixture was first filtered through Celite, then through a 0.22 μm membrane to remove insoluble components. Residual solvents were removed by evaporation under vacuum, leaving FHOA as yellow semisolid with a yield of 89±4 % (1.06 g, *n*=3). HRMS (*m/z*, ESI-TOF) for [M+2H]²⁺ was calculated to be 911.1268 and 911.1267 was measured. ¹H NMR (400 MHz, CDCl₃) δ 3.93 (t, *J* = 8.38 Hz, 8H), 2.93 – 2.61 (m, 12H), 2.56 – 2.30 (m, 20H). ¹⁹F NMR (376 MHz, CDCl₃) δ -80.81 – 81.56 (m, -CF₃, 12F), -114.40 – -114.86 (m, -CH₂CF₂-, 8F), -122.11 – -122.91 (m, 8F), -122.91 – -123.35 (m, 8F), -123.38 – -123.95 (m, 8F), -125.52 – -127.00 (m, 8F). ¹³C NMR (101 MHz, CDCl₃) δ 173.26 (C=O), 124.12 – 100.03 (m, -CF₂-, weak), 53.32, 49.90, 40.48, 29.73, 27.97 (m, -CH₂CF₂-), 24.27.

Nanoemulsion Formulation

A lipid film was prepared by dissolving 115.5 mg egg lecithin (60%, Alfa Aesar, Haverhill, MA), 9.3 mg cholesterol (Anatrace, Maumee, OH) and 16.8 mg DSPE-mPEG(2000) (Avanti Polar Lipids, Alabaster, AL) in chloroform (1.5 mL), followed by rotatory evaporation under N₂ flow, and drying under high vacuum for 24 h. The lipid film was hydrated with purified water (4.8 mL), vortexed at high for 2 min and probe sonicated for 2 mins (Omni Ruptor 250 W, 30% power, Omni International, Tusla, OK). FHOA (1 mM, 2.2 mg) was fully dissolved in PFOB or PFCE (1.2 mL)

oil and was added, and the final mixture was vortexed and sonicated sequentially for 2 min each. The pre-emulsion obtained was passed five times through a microfluidizer (LV1, Microfluidics, Newton, MA) operating at 20,000 psi and filtered through a 0.8/0.2 μm Supor membrane (Port Washington, NY) into sterile glass vials. The vials were sealed and stored at 4 °C before use. Nanoemulsion containing a higher concentration of FHOA (10 mM, 22 mg) was prepared in the same way to study the binding behavior by NMR and UV-Vis. Blank PFOB nanoemulsion was formulated in a similar way, except that no FHOA was added. FERM nanoemulsion using a polymeric surfactant (Pluronic F68) was prepared by mixing an aqueous solution of Pluronic F68 (4.8 mL, 31 g/L) with PFCE (1 mM FHOA, 1.2 mL) directly, followed by sonication and microfluidization as stated above. No phase separation was observed for >2 months of storage at 4 °C for all nanoemulsions prepared.

Metal Binding

Direct binding of ZrCl_4 to FHOA in solution was characterized by NMR spectroscopy. 0-2 equivalents of 40 mM ZrCl_4 in CD_3OD were titrated into 0.4 mL of 0.2 mM FHOA in CD_3OD in 5 mm NMR tubes. Samples were incubated at room temperature for 1 hour prior to acquisition of ^1H and ^{19}F NMR spectra. To determine binding kinetics, ^{19}F NMR spectra were recorded at 10, 20 and 30 min timepoints after addition of 1 equivalent of ZrCl_4 .

Binding and transmetallation of Zr^{4+} and Fe^{3+} to FHOA was observed by UV-vis spectroscopy and ^{19}F T_1 relaxation time measurements. 0.16 μmol of FeCl_3 or ZrCl_4 in 90% $\text{H}_2\text{O}/10\%$ D_2O was added to 40 μL of FERM nanoemulsion in 260 μL of $\text{H}_2\text{O}/10\%$ D_2O . After incubation for 3 hours, ^{19}F T_1 's were determined using inversion recovery experiments, and UV-vis spectra recorded. To investigate transmetallation, an equal amount of ZrCl_4 or FeCl_3 was added

to Fe and Zr bound emulsions, respectively, and T_1 and UV-vis measurements were repeated 16 h after addition. To determine transmetallation rate, UV-Vis spectra were also recorded every 5 min automatically in the 16 h period following addition of $ZrCl_4$ to Fe-saturated nanoemulsion.

Radiolabeling of FERM Nanoemulsion

For radiolabeling, 29.6 MBq of $^{89}ZrCl_4$ (~5 μ L in 1M HCl) was added to 1 mL of FERM nanoemulsion and gently mixed in a vial. After incubation at room temperature for 3 h, the mixture was desalted into 10 mM Tris-HCl buffer (pH=8.0) containing 2% (v/v) of propylene glycol using a Sephadex G-25 gel filtration column (NAP-10, GE Healthcare, Chicago, IL) and collected in a glass vial. The nanoemulsion was typically adjusted to a concentration of 3.7 MBq per 0.2 mL with Tris buffer for *in vivo* injection. The radiolabeling yield of FERM was calculated from the ratio of activity in the collected eluate to total activity. A prolonged reaction time (16 h) did not significantly increase the yield. Quantitative ^{19}F NMR from decayed samples showed a typical recovery of $61.2 \pm 8.0\%$ (0.8 mL, n=3) of total fluorine atoms loaded into the column.

For radiolabeling with ^{89}Zr -oxalate (in 1 M oxalic acid), 22.2 MBq (~10 μ L) of ^{89}Zr -oxalate in 30 μ L 1 M $NaHCO_3$, and 10 μ L 1 M Tris buffer (pH=8.0) was added to 1 mL of lipid FERM nanoemulsion, which resulted in a final pH between 6-6.5 as tested by pH paper. After incubation at room temperature for 3 h, the mixture was desalted using the above method.

MTT Assay

The murine macrophage cell line RAW264.7 (ATCC, Manassas, VA) was maintained in DMEM containing 10% fetal bovine serum (FBS), 10 mM HEPES, 1 mM sodium pyruvate, and 1.5 g/L sodium bicarbonate at 37 °C in 5% CO_2 atmosphere. Cells were grown in 10 mL cell culture tubes.

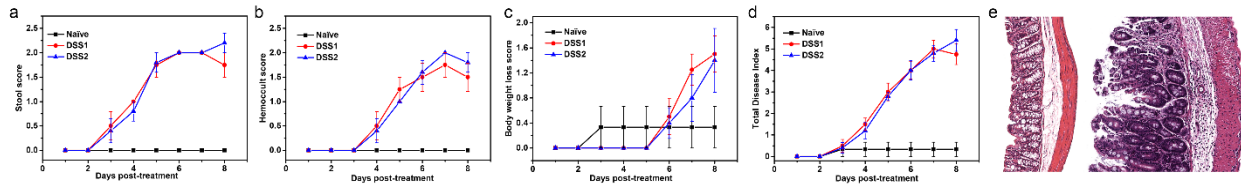
Nanoemulsion with FHOA (1 mM in oil) or without chelate were added at a fluorine concentration of 5 mg/mL overnight. Cells without nanoemulsion labeling were used as control groups. After incubation overnight at 37 °C, cells were washed three times in PBS and counted using a Countess II FL Automated Cell Counter (Fisher Scientific, Waltham, WA). The labeled and unlabeled cells were seeded in 96-well plate with 10⁵/well in cell culture medium. An MTT assay kit (ab211091, Abcam, Cambridge, UK) was used following the manufacturer’s protocol at 0, 18, 24, and 48 hours. The absorbance at OD=590 nm was measured using an Infinite 200 plate reader (Tecan, Männedorf, Switzerland).

Supplemental Table

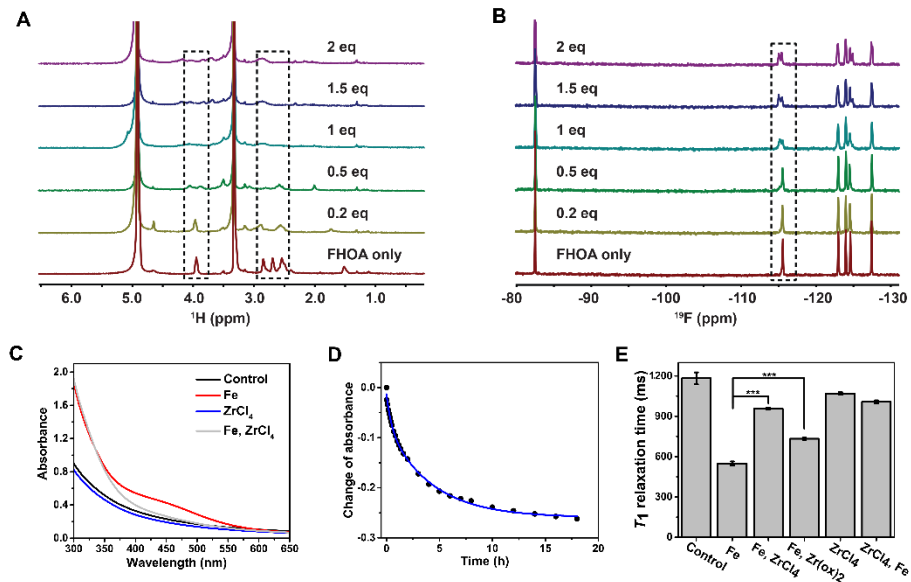
Oil	Surfactant	Size (nm)	PDI	¹⁹F (mg/mL)
PFOB Blank	Lipids	162.0 ± 7.7	0.045 ± 0.031	179.9 ± 6.6
PFOB-FHOA	Lipids	158.0 ± 1.9	0.085 ± 0.006	168.5 ± 5.8
PFCE-FHOA	Lipids	151.8 ± 4.7	0.073 ± 0.030	154.1 ± 9.0
PFCE-FHOA	Pluronic F68	137.3 ± 6.6	0.084 ± 0.052	161.2 ± 6.1

Supplemental Table 1. FERM nanoemulsion size and polydispersity index (PDI), measured by DLS, for various formulations with different fluorocarbons and surfactants types. The fluorine content of prepared nanoemulsions were assayed using ¹⁹F NMR. Data are shown as mean ± standard error (n=3).

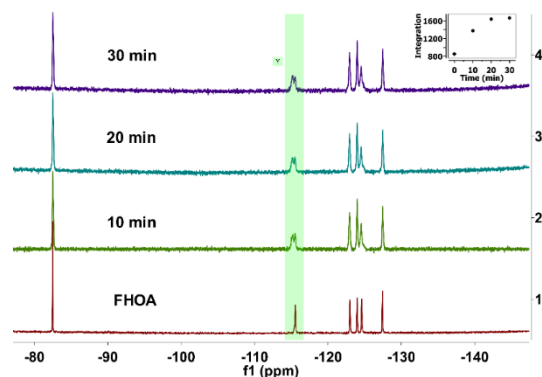
Supplemental Figures



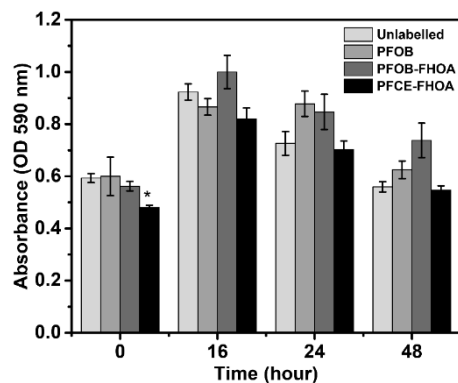
Supplemental Fig. 1. Characterization of dextran sulfate sodium (DSS) treated IBD C57BL/6 mouse model. Control mice (naïve, n=3) were fed with regular water, while IBD mice were fed with water containing 3% DSS (groups DSS1, n=4; DSS2, n=5) for 8 days before imaging. Panel (a) shows stool consistency score (0=normal, 1=soft but still formed, 3=very soft, 4=diarrhea). In (b), hemocult scores are shown (0=negative, 1=positive, 2=visible traces of blood, 3=gross rectal bleeding). (c) Displays body weight loss score (0 for 0-1% body weight loss, 1 for 1-5% loss, 2 for 5-10% loss, 3 for 10-20% loss and 4 for >20% loss). (d) Represents total disease index, defined as the summation of scores from (a)-(c). Two mice from DSS1 group and three mice from DSS2 group were used for imaging studies. Panel (e) displays representative H&E-stained sections from Swiss rolls made from colon of an untreated mouse (left) and a mouse treated with DSS (right). The DSS colon (right) displays pronounced inflammation characterized by mucosal hyperplasia, goblet cell depletion and mononuclear cell infiltration. The fixed segments (2% PFA) were embedded in paraffin, cut into 5 μm -thick transverse sections, and stained with hematoxylin and eosin (H&E) and imaged (200 \times).



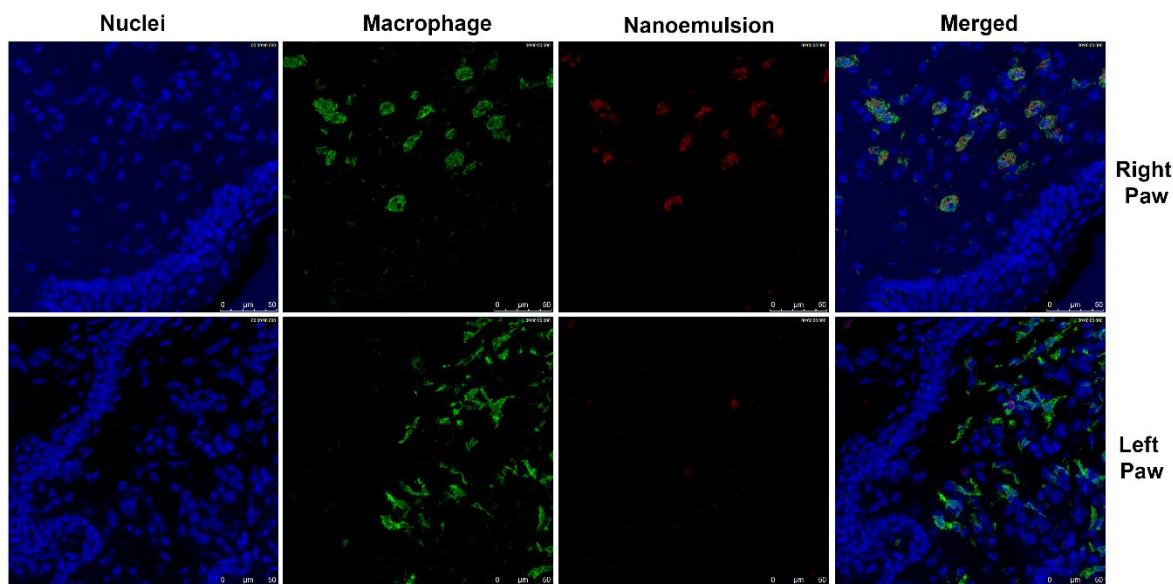
Supplemental Fig. 2. Metal-binding properties of FERM nanoemulsion. (A, B) Display changes in ^1H and ^{19}F NMR spectra with binding between FHOA and Zr^{4+} (non-radioactive) in CD_3OD at varying doses. Panel (C) shows UV-Vis spectra of nanoemulsion with addition of Zr^{4+} (2eq) or Fe^{3+} (2eq). Adding Zr^{4+} to the Fe-bound FERM nanoemulsion (red line) causes a decrease in absorbance at ~ 450 nm (grey line). “Control” is FERM nanoemulsion without metal (black line). Panel (D) displays UV-Vis absorbance at 450 nm over time after adding Zr^{4+} (2 eq) to Fe-bound FERM nanoemulsion; a bi-exponential fit yields $t_{1/2}$ values of 0.32 ± 0.07 h and 2.91 ± 0.26 h, with $R^2 = 0.9971$. In (E), we show the ^{19}F T_1 of PFOB ($-\text{CF}_2\text{Br}$ peak) nanoemulsion upon metal binding. Data are mean \pm s.e.m. ($n=3$), where *** denotes $P < 0.001$ for unpaired t-tests.



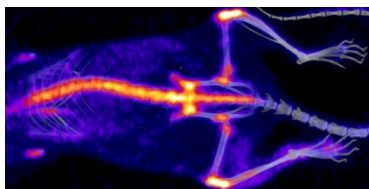
Supplemental Fig. 3. Time-lapse ^{19}F NMR spectra of FHOA upon addition of ZrCl_4 (1 eq, non-radioactive). The insert (upper right) shows the integration values of peaks centered at -115.8 ppm at each time point.



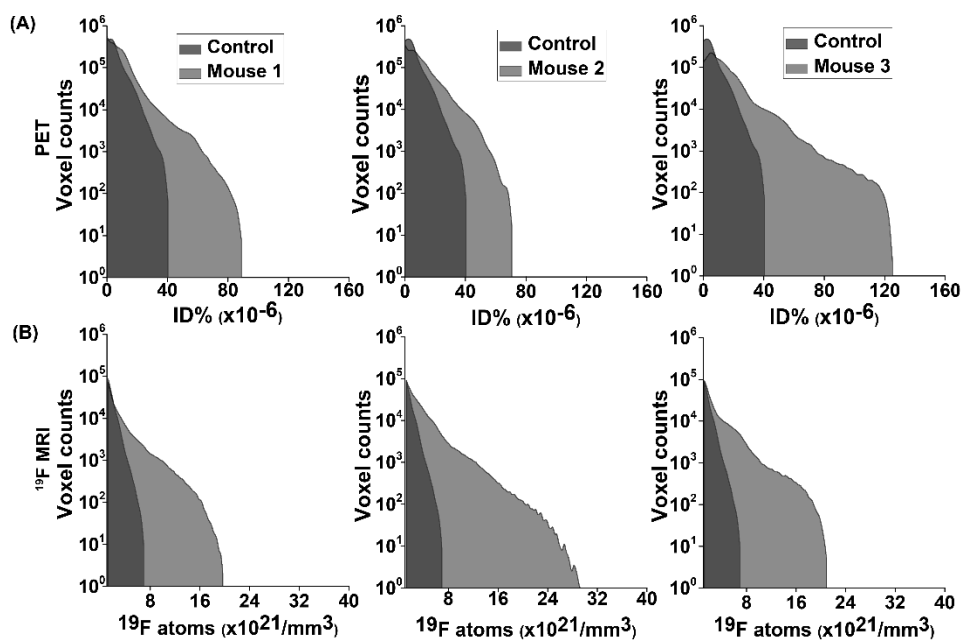
Supplemental Fig. 4. Cytotoxicity in RAW264.7 cells labeled overnight with FERM nanoemulsion (PFOB or PFCE), measured by the MTT assay over 48 hours. Data are shown as mean \pm standard error (n=3). Unpaired t-test analyses show insignificant differences between nanoemulsion labeled groups and unlabeled groups ($p > 0.05$), except for PFCE-FHOA at 0 h where $p < 0.05$ (*).



Supplemental Fig. 5. Representative immunofluorescence confocal images of mouse paw sections from λ -carrageenan inflammation model. Data show the colocalization of fluorescent fluorocarbon nanoemulsion (red) with macrophages (green) in the inflamed, right paw and absence of nanoemulsion in the (control) left paw. We employed a dual-mode fluorocarbon nanoemulsion containing a red-fluorescent dye (VS-1000H DM Red, 150 nm droplet size, Celsense, Pittsburgh, PA). The nanoemulsion was injected through tail vein of mice bearing inflammation on the right paw (n=3). After 24 h, mice were sacrificed and paws were harvested, weighted, cryo-frozen in optimal cutting compound and kept frozen at $-80\text{ }^{\circ}\text{C}$. Nuclei are stained with Hoechst (blue, 62249, Thermo Fisher). The sections were cut along the palm direction at $10\text{ }\mu\text{m}$ thickness in a cryotome and fixed with 4% paraformaldehyde, followed by permeabilization and Fc blocking. Slices were stained with rabbit anti-mannose receptor (ab64693, Abcam, Cambridge, UK) as primary antibody and Alexa Fluor 488 goat anti-rabbit (A11008, Thermo Fisher) as the secondary antibody. Confocal images (CTR 6500, Leica Microsystems, Buffalo Grove, IL) were acquired of sections at $63\times$ magnification. Scale bar = $50\text{ }\mu\text{m}$.



Supplemental Fig. 6. Representative PET/CT image of mouse 24 h after injected with free $^{89}\text{ZrCl}_4$ (3.7 MBq in 0.2 mL Tris buffer). The image data is displayed as a maximum-intensity projection.



Supplemental Fig. 7. PET (A) and ^{19}F MRI (B) histograms of nanoemulsion quantification per voxel are shown for abdominal ROI encompassing entire peritoneum of IBD mice or control mice. Images for these mice are displayed in manuscript Fig. 3.